24. Vogt, S. S. *et al.* Five new multicomponent planetary systems. *Astrophys. J.* **632**, 638–658 (2005).
25. Mayor, M. *et al.* The CORALIE survey for southern extrasolar planets. XII. Orbital solutions for 16 extrasolar planets discovered with CORALIE. *Astron. Astrophys.* **415**, 391–402 (2004).
26. Beaulieu, J.-P. *et al.* in *Second Eddington Workshop: Stellar Structure and Habitable Planet Finding* (eds Favata, F., Aigrain, S. & Wilson, A.) 177–182 (ESA SP-538, ESA Publications Division, Noordwijk, 2004).
27. Moutou, C. *et al.* Comparative blind test of five planetary transit detection algorithms on realistic synthetic light curves. *Astron. Astrophys.* **437**, 355–368 (2005).
28. Sozzetti, A. *et al.* Narrow-angle astrometry with the space interferometry mission: the search for extrasolar planets. I. Detection and characterization of single planets. *Pub. Astron. Soc. Pacif.* **114**, 1173–1196 (2002).
29. Bennett, D. P. in *ASP Conf. Ser. on Extrasolar Planets: Today and Tomorrow* (eds Beaulieu, J.-P., Lecavelier des Etangs, A. & Terquem, C.) Vol. 321, 59–68 (ASP, 2004).
30. Beaulieu, J. P. *et al.* PLANET III: searching for Earth-mass planets via microlensing from Dome C? *ESA Publ. Ser.* **14**, 297–302 (2005).

Acknowledgements PLANET is grateful to the observatories that support our science (the European Southern Observatory, Canopus, Perth; and the South African Astronomical Observatory, Boyden, Faulkes North) and to the ESO team in La Silla for their help in maintaining and operating the Danish telescope. Support for the PLANET project was provided by CNRS, NASA, the NSF, the LLNL/NNSA/DOE, PNP, PICS France-Australia, D. Warren, the DFG, IDA and the SNF. RoboNet is funded by the UK PPARC and the FTN was supported by the Dill Faulkes Educational Trust. Support for the OGLE project, conducted at Las Campanas Observatory (operated by the Carnegie Institution of Washington), was provided by the Polish Ministry of Science, the Foundation for Polish Science, the NSF and NASA. The MOA collaboration is supported by MEXT and JSPS of Japan, and the Marsden Fund of New Zealand.

Author Information The photometric data set is available at planet.iap.fr and ogle.astrouw.edu.pl Reprints and permissions information is available at npg.nature.com/reprintsandpermissions. The authors declare no competing financial interests. Correspondence and requests for materials should be addressed to J.P.B. (beaulieu@iap.fr) or D.P.B. (bennett@nd.edu).

Vol 439|26 January 2006|doi:10.1038/nature04400 nature

LETTERS

Laser acceleration of quasi-monoenergetic MeV ion beams

B. M. Hegelich[1], B. J. Albright[1], J. Cobble[1], K. Flippo[1], S. Letzring[1], M. Paffett[1], H. Ruhl[2], J. Schreiber[3,4], R. K. Schulze[1] & J. C. Fernández[1]

Acceleration of particles by intense laser–plasma interactions represents a rapidly evolving field of interest, as highlighted by the recent demonstration[1–4] of laser-driven relativistic beams of monoenergetic electrons. Ultrahigh-intensity lasers can produce accelerating fields of 10 TV m^{-1} (1 TV = 10^{12} V), surpassing those in conventional accelerators by six orders of magnitude. Laser-driven ions with energies of several MeV per nucleon have also been produced[5–9]. Such ion beams exhibit unprecedented characteristics—short pulse lengths, high currents and low transverse emittance[10]—but their exponential energy spectra have almost 100% energy spread. This large energy spread, which is a consequence of the experimental conditions used to date, remains the biggest impediment to the wider use of this technology. Here we report the production of quasi-monoenergetic laser-driven C^{6+} ions with a vastly reduced energy spread of 17%. The ions have a mean energy of 3 MeV per nucleon (full-width at half-maximum ~0.5 MeV per nucleon) and a longitudinal emittance of less than 2 × 10^{-6} eV s for pulse durations shorter than 1 ps. Such laser-driven, high-current, quasi-monoenergetic ion sources may enable significant advances in the development of compact MeV ion accelerators[11], new diagnostics[12,13], medical physics[14], inertial confinement fusion and fast ignition[15–17].

An ultrahigh-intensity laser ($I\lambda^2 > 10^{18}$ W cm^{-2} μm^2, where I is intensity and λ is wavelength) incident on a target accelerates a large number of electrons to multi-MeV energies[18,19]. These electrons traverse typical thin foil targets and set up a very strong electrostatic field exceeding 1 TV m^{-1}. This field ionizes the rear surface and accelerates ions to energies of many MeV. This process is known as target normal sheath acceleration (TNSA)[5]. Experiments have demonstrated acceleration of protons to more than 60 MeV (ref. 8), fluorine ions to above 100 MeV (ref. 6) and high-Z palladium ions up to 225 MeV (ref. 20), that is, more than 2 MeV per nucleon. These ion beams have a much lower transverse temperature and a much shorter duration and a much higher current than those from conventional accelerators. These unique characteristics make them ideal candidates for a number of experiments not feasible otherwise.

Owing to their short pulse length and high energy content, the ion beams can heat macroscopic amounts of matter to more than 10^6 °C before the matter can expand[21], thereby creating conditions of high temperature and density only found in the interior of stars. Conversely they can also be used as a probe to investigate ion transport and stopping in a hot, dense plasma before it has time to disassemble. Conventional accelerators are hard pressed to deliver enough particles in the available ~ps time window to make high-quality measurements feasible. These are but two examples where the high current and short pulse duration are the key to an otherwise impossible experiment. More examples can be found in nuclear physics, fusion research and other areas—examples are the synthesis of neutron rich nuclei or the measurement of fusion cross-sections in supernova-like hot, dense plasma conditions. The much higher beam current and the much lower emittance of the laser-driven ion beams make them a promising candidate for advanced accelerator concepts.

Today, a standard linear accelerator that matches the MeV/u energy level (with u being the atomic mass unit) of these laser-driven ions is ~100 m long. In contrast, the laser fits in a large room and accelerates the ions to MeV/u over just 10 μm. The low duty-cycle in present experiments is a limitation that is likely to be mitigated by the next generation of high-power lasers, currently under development. However, the major difficulty with all the TNSA and other laser-driven ion-acceleration mechanisms[9,22] has been the resulting maxwellian energy distribution, with a typical 100% energy spread[6,9]. All the above-mentioned applications would benefit greatly from a narrower energy distribution, centred about a specific value.

We report here a laser-driven quasi-monoenergetic ion beam, a

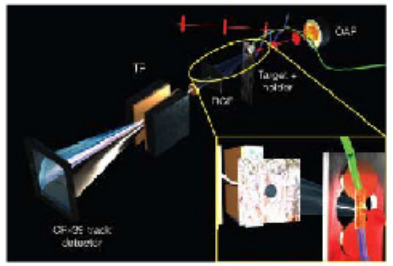

Figure 1 | Experimental set-up. A short, high-intensity laser pulse is focused on a thin metal foil target by an off-axis parabolic mirror (OAP). The red line shows the laser beam axis, and the red disks represent the laser pulse travelling along that axis and getting focused down by the OAP. Two wires (green and blue) are attached to the target, pass a current through it and heat it to ~1,100 K to remove contaminants. Ions are accelerated at the target rear surface and are detected by a stack of radiochromic film (RCF) and a Thomson parabola (TP) spectrometer using CR-39 track detectors. The inset shows an enlarged frontside view of the target, with the target and the green and blue wires being in the lower right corner and the RCF and TP detectors in the upper left.

[1]Los Alamos National Laboratory, Los Alamos, New Mexico 87545, USA. [2]University of Nevada, Reno, Nevada 89557, USA. [3]Ludwig-Maximilian-Universität Muenchen, [4]Max-Planck-Institut für Quantenoptik, Garching 85748, Germany.

C^{5+} beam created in the interaction of a 20 TW/0.8 ps laser pulse with a solid target. A simple schematic illustrating the process can be found in Supplementary Information (sections SI_1 and SI_2). The experiments were performed at the LANL Trident laser facility. The experimental set-up is shown in Fig. 1 (for details see Methods), and a time-integrated photograph of an actual laser shot is shown in Supplementary Information section SI_3. The monoenergetic signature is the direct result of a fundamentally different target composition employed in these experiments. In TNSA, the ions with the highest charge-to-mass ratio dominate the acceleration, gaining the most energy. Given typical vacuum conditions of $\sim 10^{-6}$ mbar, surface target contaminants containing protons are always present. These protons have the largest charge-to-mass ratio by at least a factor of 2. Controlled treatment of foil targets before irradiation with the ultrahigh-intensity laser reduces adsorbed and absorbed proton contaminants to an unobservable level, allowing higher-Z ions to be the dominant species[6]. Using the right treatment parameters and target materials, a thin source layer of just a few monolayers can be formed by catalytic processes.

Specifically, we have demonstrated the acceleration of C^{5+} and C^{6+} from an ultrathin layer of graphitic carbon, formed from catalytic decomposition of adsorbed hydrocarbon impurities on a 20 μm palladium foil. Unlike the low-energy lasers which are used for electron acceleration[2–4], which have a high repetition rate and allow the taking of many shots to obtain good statistics, ion acceleration requires higher energy lasers which are single shot in nature. The number of shots is extremely limited and fluctuations in the laser parameters further complicate obtaining good statistics. However, five shots exhibiting monoenergetic carbon ions have been observed in two separate campaigns months apart, and another ten shots showing indication of monoenergetic ions are still being analysed. Figure 2 shows the measured C^{5+} spectrum (black curve) with the lowest ratio $\Delta E/E$ of ~17%, where E is the mean energy of the C^{5+} ions and ΔE is their energy spread. It also shows the corresponding highest substrate charge state Pd^{22+} (blue). Having the highest charge-to-mass ratio of 0.42, the C^{5+} is dominantly accelerated. Owing to the extremely small spatial extent of the carbon layer and its localization at the rear surface, all of the carbon ions are accelerated at once at the peak of the accelerating field, leading to the monoenergetic ion pulse. After all carbon ions are accelerated, the field is still very strong and only moderately screened by the carbon, therefore the next highest charge-to-mass ratio ion—that is, Pd^{22+} with a charge-to-mass ratio of 0.2—is now dominantly accelerated and gains a large fraction of the energy before the field decays and lower Pd charge states are created and accelerated.

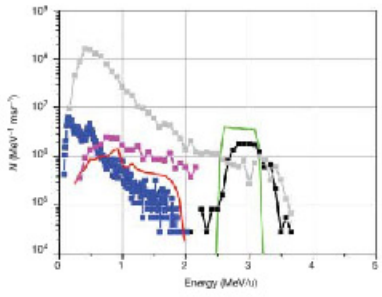

Figure 2 | Monoenergetic carbon ions from a 20 μm palladium substrate. The curves show ion number (N) over energy per nucleon (MeV/u). The black curve shows the spectra of the measured C^{5+} ions, the blue curve shows the dominant substrate charge state Pd^{22+}. The green and the red curves are simulations obtained using the 1D-hybrid-code BILBO, showing the simulated C^{5+} and Pd^{22+} spectra, respectively. The grey curve shows the dominant C^{6+} signal from a heated W target, and the magenta trace shows the C^{5+} signal from a cold Pd target. In these last two cases, the targets have a thick layer of carbon contaminants and do not form a monolayer source. The resulting carbon signals are therefore exponential and show lower numbers in the high-energy range. The errors are: $dN \leq 1\%$ statistical accuracy, and $dE \leq 2\%$ for C and $dE \leq 4.5\%$ for Pd.

For the purpose of this Letter we limit our discussion to the two dominant charge states, which together contain ~20% of the total integrated ion energy and have a bearing on the results reported here. The leading short bunch of C^{5+} ions shows a monoenergetic energy distribution with a mean energy of $E \approx 36$ MeV, that is, 3 MeV per nucleon and a full-width at half-maximum of 0.5 MeV per nucleon. We infer that the accelerated C^{5+} ion bunch has a longitudinal emittance of $\varepsilon_l < 2 \times 10^{-6}\,\pi$ eV s, improving on conventional high-current accelerators by orders of magnitude. Also, in contrast to the Pd and to any previous measurements, no lower C charge states are present. Closer analysis reveals important differences in the acceleration mechanism for the Pd substrate ions and the C ions from the source surface layer. Whereas the substrate ions have a typical exponential spectrum, the C ions are monoenergetic.

The small energy spread of the observed carbon ions can be understood from consideration of quasi-neutral ($n_e = Z_{Pd} n_{Pd}$), adiabatic expansion in one dimension (1D) of a palladium substrate coated by a very thin film of carbon. (Here n_e is the electron density, n_{Pd} the palladium density and Z_{Pd} the mean palladium charge state.) The electric field obeys $eE \approx -m_e n_e^{-1} \partial_x \int dv v^2 (f_e - Z_{Pd} f_{Pd})$, with f_e and f_{Pd} the distribution functions of electrons and palladium ions, e the elementary charge, m_e the electron mass and v velocity. Such a plasma column will expand with sound speed c_s to characteristic size $L^2(t) = L_0^2(1 + t^2 c_s^2 / L_0^2)$. The ion and electron temperatures will therefore decrease by a factor $L_0/L(t)$, which leads to an electric field $eE \approx x c_s^2 m_{Pd} Z_{Pd}^{-1} L^{-1}$, where m_{Pd} is the atomic mass of palladium. This field leads to an acceleration $d^2x_C/dt^2 = r x_C c_s^2 L^{-2}$ of the carbon ions, with x_C being the spatial coordinate of the carbon ions. The dynamics of the layer are characterized by r, the ratio of charge-to-mass ratios of C to Pd ions: for $r \gg 1$, the carbon layer detaches from the substrate at early time and propagates ahead of it as a directed bunch. For $r < 1$, the substrate overtakes the C layer and flow instabilities may arise. With an average Pd charge state $Z_{eff,Pd} \approx 7$, one obtains $r = 6.3$, predicting a clean separation of

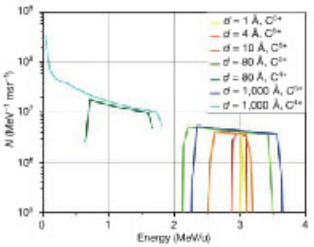

Figure 3 | Changing the thickness of the carbon source layer leads to a change in the energy spectrum in the BILBO simulations. Decreasing the layer thickness (d) causes the spectrum to become more monoenergetic. Increasing the layer thickness leads to a broader distribution and ultimately the appearance of lower charge states and a maxwellian spectrum.

the carbon ions from the substrate. Esirkepov *et al.*[23] have also examined the problem of monoenergetic ion acceleration, but their model relies explicitly upon finite transverse extent of the target and is not applicable to the TNSA scenario we find in our experiments.

In order to improve our understanding and our predictive capability, we developed a numerical model that simulates the ionization and acceleration physics. Full *ab initio* simulations with the required dynamics and sufficiently low noise levels to faithfully capture the ionization kinetics are not feasible, so we have focused on a reduced model that takes into account the essential physics. This 1D-hybrid model BILBO (backside ion lagrangian blow-off) uses a relativistic Boltzmann fluid model of the electrons and represents ions as kinetic simulation particles. This model has been explicitly designed to implement TNSA[5] in a heterogeneous mixture of ionization species and ion types. In our simulations, a thin layer of carbon (1–1,000 Å) with areal density $\rho = 5 \times 10^{-10}$–5×10^{-7} g cm^{-2} is placed on the surface of a palladium foil of solid density $\rho = 12.16$ g cm^{-3} and a thickness of 20 μm. Using parameters matched to the experiment (see Methods), we are able to reproduce the experimental results.

Figure 2 shows the energy spectra of the C^{5+} (green) and Pd^{21+} (red) components obtained in the simulation. The energy per nucleon of the C^{5+} ions agrees well with the measured energies and the total number of ions accelerated, albeit with a somewhat smaller energy spread. The energy spectrum and peak ionization state of Pd between 50 and 200 MeV are likewise in good agreement with the data. From this simulation we can also infer a source layer thickness of ~10 Å (that is, a few monolayers), which is in good agreement with published measurements—for example, using Auger spectroscopy[24,25]. In our parametric simulation study, increasing the number of initial carbon layers while keeping the density fixed leads to two effects, shown in Fig. 3. The mean energy of the C^{5+} beam decreases and the energy spread increases with increased layer thickness. This trend continues until adequate space charge exists in the carbon layer to shield the ionizing electric field experienced by the carbon ions at the back of the layer. These more deeply buried carbon ions only attain ionization state C^{4+} and they separate from the layer of C^{5+} ions; for the parameters considered in this study, this occurs for areal charge densities exceeding $\sim 2 \times 10^{-8}$ g cm^{-3}, corresponding to a layer thickness of ~80 Å and above. Lower carbon ionization states appear with increasing layer thickness, and the ion energies eventually approach a maxwellian distribution. This behaviour is also seen in the experiment (Fig. 2). The grey curve shows the C^{6+} spectrum from a laser shot of comparable energy but from a tungsten target, which is not a catalyst for the required surface chemistry, and therefore does not form a thin source layer.

Measurements using transmission electron microscopy (see Supplementary Information section SI_4) reveal that upon heating, the target actually forms a 400-Å-thick tungsten carbide (W_2C) layer. This surface layer is not thin enough, and as a consequence the C spectrum is maxwellian and all lower charge states are present, as observed in earlier experiments[6]. Comparison of the two spectra shows that the direct production of monoenergetic ions by thin source layers is more effective than just slicing the equivalent energy range out of the maxwellian spectrum. Specifically, the number of ions in the corresponding energy range from 2.5 to 3.5 MeV per nucleon is a factor of 2 lower than in the monoenergetic case. Comparison with a cold Pd target shot at similar laser conditions also shows a maxwellian distribution of considerable lower energy (magenta curve, Fig. 2), because (1) the protons drain energy, and (2) the localized source layer is not formed. Our model predicts that the energy spread in the carbon beam may be minimized by localizing the initial carbon layer spatially, that is, by minimizing the source layer thickness, a process which should also result in higher mean energy of the light ion beam. This hypothesis will be tested in future experiments.

Our experimental results, simulation and analytic modelling have established the basis for laser-driven acceleration of monoenergetic ion beams using specifically designed and treated targets. Moreover, catalytic metal substrates such as Pd offer the chance of having a target that configures itself *in situ* if subjected to the right conditions. Such a target would solve major technical obstacles for a host of possible applications, making future laser-based accelerators much more feasible. We recently confirmed these results by repeating the experiments in another campaign at the Trident facility, using a substantially equivalent experimental set-up, where we reproduced the qualitative findings reported here. Although the errors in the analysis for any specific shot are small, the reproducibility of our C^{5+} results from shot to shot is only ~50%, possibly owing to the degree of control and diagnosis of key input parameters achievable in our present experimental set-up. Large, high-energy, single-shot glass lasers have typical shot-to-shot power fluctuations of ~25%, and the focal spot conditions drift over time. Varying preplasma conditions and possible self-focusing add further to the variability of the results.

The resulting unique beam characteristics, including short pulse duration, high current and small transverse and longitudinal emittances, represent a strong incentive to pursue further research and applications, such as advanced accelerator concepts[11], laboratory astrophysics, isochoric heating[21], fusion science[15] and medical physics[14]. The achieved particle energy is already in the right energy range for fusion applications like fast ignition, whereas particle number and conversion efficiency have to be substantially increased. For medical applications like tumour therapy the situation is the opposite: here, the particle numbers are sufficient but the particle energy has to be increased substantially. Considering the fast paced progress in ultrahigh intensity laser technology in recent years, it is reasonable to anticipate progress on all these issues and the deployment of a laser-driven, quasi-monoenergetic ion accelerator in the not so distant future. Progress made in diode-pumped glass laser systems, especially, should enable far higher repetition rates of 0.1–1 Hz (ref. 26). At these repetition rates, several applications in accelerator physics, medical physics, material science and neutron physics become feasible.

METHODS

Laser system and diagnostics. The experiments were performed at the short pulse arm of the Trident Nd:glass laser facility at Los Alamos National Laboratory. The Trident C-beam delivers up to 30 TW in a 20 f, ~600 fs pulse at 1.054 μm wavelength, using chirped pulse amplification[27]. The typical pulse contrast is $\sim 10^{-6}$ at 2 ns before the peak of the pulse. As illustrated in Fig. 1, an off-axis parabolic mirror is used to focus the laser pulse onto a thin foil target at 22.5° with respect to the target normal. Typical focal spot sizes are ~10 μm radius, resulting in intensities on target of $\sim 10^{19}$ W cm^{-2}. A stack of Gafcom radiochromic film (RCF) is placed behind the target to record the ion beam profile. A hole in the middle of this film stack provides a line of sight for a Thomson parabola (TP) ion spectrometer[28] attached to the outer chamber wall. The Thomson parabola deflects the ions by means of parallel electric and magnetic fields, so that the projection of their path in the detector is defined by parabolic traces. Ions with different charge-to-mass ratios are deflected onto different traces, while their positions on a given trace are determined by their energies. A CR-39 solid state nuclear track detector records the ions, typically ~300,000 per shot, and is read out by a specialized automated analysis system[29]. With properly chosen parameters, the counting error is below 0.01%. The error in ion numbers per energy bin (dN) is dominated by Poisson statistics, and is below ≤1% owing to the large number of counts per shot. For example, for the C^{5+} trace in Fig. 2, $dN \approx 0.3\%$. The solid angles of the TPs are 3.4×10^{-5} millisteradians (msr), and the opening angles of the ion beams are 24–100 msr depending on charge state and energy. The TPs are absolutely calibrated for energy and the energy error is dominated by the pinhole size (100 μm). It is given as $dE \sim E^{3/2}$, yielding an upper boundary for an energy error of less than 1 MeV for ~45 MeV carbon, that is, less than 2% and decreasing with energy.

Target treatment and chemistry. The foil target is heated to $T_1 \approx 1{,}100$ K by two attached wires that pass a current through the foil. Palladium at room temperature is a hydrogen-getter, that is, H can be found throughout the bulk of the material as well as on the surfaces. The heating process desorbs the hydrogen contaminants (adsorbed and absorbed in the foil), thus enabling the efficient acceleration of heavier ions. In the experiment presented here, the special

catalytic surface chemistry of palladium causes a few carbon monolayers of hydrocarbon contaminants to remain on the surface of the palladium substrate and form a well defined source layer for the monoenergetic carbon beam. Given the ambient vacuum of $\sim 10^{-6}$ mbar, the surface is contaminated with various C_xH_y compounds. When the Pd is heated, the Pd surface undergoes multiple phase changes[21,22] and the loosely bound H is driven out of the bulk and off the surfaces. At 600 K the target is completely dehydrogenized. The carbon, however, remains on the surface in various different configurations. When heating the target further, to temperatures $T > 1{,}100$ K, the various carbon compounds undergo a phase change, forming a well-defined, very thin graphite layer at the monolayer scale on the Pd surface. If heated up further, to above 1,300 K, this layer will be removed and a clean Pd surface remains. In the experiment, we did not reach this last state, but remained in the graphite regime, thereby preparing a thin source layer perfect for creating monoenergetic ions.

BILBO hybrid code. In BILBO, ion formation and acceleration is accomplished by the electric fields of a virtual cathode of hot electrons at the back surface of the target. Assuming separation of the electron and ion timescales, self-consistent electric fields are obtained by solving the time-stationary relativistic Vlasov–Maxwell equations for each electron component. These fields accelerate the ions and ionize them to higher charge states, where ionization is implemented in BILBO by means of a threshold ionization model[36]. The boundary conditions require the electric field to vanish within the target and far from the target surface. In addition, the electron densities and temperatures of the hot and cold components are specified within the target as internal boundary conditions. The hot electron density and temperature are functions of the laser energy deposition model, and their dynamics include adiabatic expansion and the loss of energy to ionization and ion acceleration. The cold electron temperature increases from ohmic heating and collisions with the hot electron component. In the simulations, the laser spot diameter was assumed to be 30 μm; 50% absorption of the incident laser into hot electrons was assumed ($T_h = 2.5$ MeV), with the hot electrons' density assumed to be equal to the critical density ($n_e = 1.01 \times 10^{21}$). The cold electrons had $n_c = 6.8 \times 10^{22}$ cm^{-3} and initial cold electron temperature $T_c = 10$ eV. The density and temperature profiles of the hot electron component were assumed to evolve in time with gaussian shape during the pulse rise and have a full-width at half-maximum of 700 fs. The simulation used 5×10^4 simulation ions of each species, had a time step of 2 fs, and employed 6×10^5 simulation cells over a domain of size 100 μm.

Received 17 August; accepted 3 November 2005.

1. Kaitsouleas, T. Accelerator physics: Electrons hang ten on laser wake. *Nature* **431**, 515–516 (2004).
2. Faure, J. *et al.* A laser–plasma accelerator producing monoenergetic electron beams. *Nature* **431**, 541–544 (2004).
3. Mangles, S. *et al.* Monoenergetic beams of relativistic electrons from intense laser–plasma interactions. *Nature* **431**, 535–538 (2004).
4. Geddes, C. *et al.* High-quality electron beams from a laser wakefield accelerator using plasma-channel guiding. *Nature* **431**, 538–541 (2004).
5. Hatchett, S. *et al.* Electron, photon, and ion beams from the relativistic interaction of Petawatt laser pulses with solid targets. *Phys. Plasmas* **5**, 2076–2082 (2000).
6. Hegelich, M. *et al.* MeV ion jets from short-pulse-laser interaction with thin foils. *Phys. Rev. Lett.* **89**, 085002 (2002).
7. Roth, M. *et al.* Energetic ions generated by laser pulses: A detailed study on target properties. *Phys. Rev. Spec. Topic Accelerators Beams* **5**, 061002 (2002).
8. Snavely, R. *et al.* Intense high-energy proton beams from petawatt-laser irradiation of solids. *Phys. Rev. Lett.* **85**, 2945–2948 (2000).
9. Maksimchuk, A., Gu, S., Flippo, K., Umstadter, D. & Bychenkov, V. Yu. Forward ion acceleration in thin films driven by a high-intensity laser. *Phys. Rev. Lett.* **84**, 4108–4111 (2000).
10. Cowan, T. *et al.* Ultralow emittance, multi-MeV proton beams from a laser virtual-cathode plasma accelerator. *Phys. Rev. Lett.* **92**, 204801 (2004).
11. Habs, D., Pretzler, G., Pukhov, A. & Meyer-ter-Vehn, J. Laser acceleration of electrons and ions and intense secondary particle generation. *Prog. Part. Nucl. Phys.* **46**, 375–377 (2001).
12. Cobble, J. A., Johnson, R. P., Cowan, T. E., Renard-Le Galloudec, N. & Allen, M. High resolution laser-driven proton radiography. *J. Appl. Phys.* **92**, 1775–1779 (2002).
13. Borghesi, M. *et al.* Proton imaging: a diagnostic for inertial confinement fusion/fast ignitor studies. *Plasma Phys. Control Fusion* **43**, A267–A276 (2001).
14. Ledingham, K. *et al.* High power laser production of short-lived isotopes for positron emission tomography. *J. Phys. D* **37**, 2341–2345 (2004).
15. Kodama, R. *et al.* Fast heating of ultrahigh-density plasma as a step towards laser fusion ignition. *Nature* **412**, 798–802 (2001).
16. Roth, M. *et al.* Fast ignition by intense laser-accelerated proton beams. *Phys. Rev. Lett.* **86**, 436–439 (2001).
17. Temporal, M., Honrubia, J. J. & Atzeni, S. Numerical study of fast ignition of ablatively imploded deuterium–tritium fusion capsules by ultra-intense proton beams. *Phys. Plasmas* **9**, 3098–3107 (2002).
18. Wilks, S. *et al.* Energetic proton generation in ultra-intense laser–solid interactions. *Phys. Plasmas* **8**, 542–549 (2001).
19. Atzeni, S. & Meyer-ter-Vehn, J. *The Physics of Inertial Confinement Fusion* (Oxford Univ. Press, Oxford, 2004).
20. Hegelich, M. *et al.* Spectral properties of laser-accelerated mid-Z MeV/u ion beams. *Phys. Plasmas* **12**, 056314 (2005).
21. Patel, P. *et al.* Isochoric heating of solid-density matter with an ultrafast proton beam. *Phys. Rev. Lett.* **91**, 125004 (2003).
22. Gitomer, S. J. *et al.* Fast ions and hot electrons in the laser-plasma interaction. *Phys. Fluids* **29**, 2679–2688 (1986).
23. Esirkepov, T. Zh. *et al.* Proposed double-layer target for the generation of high-quality laser-accelerated ion beams. *Phys. Rev. Lett.* **89**, 175003 (2002).
24. Hamilton, J. C. & Blakeley, J. M. Carbon segregation to single crystal surfaces of Pt, Pd and Co. *Surf. Sci.* **91**, 199–217 (1980).
25. Ramsier, R. D., Lee, K.-W. & Yates, J. T. Jr A sensitive method for measuring adsorbed carbon on palladium surfaces: Titration by NO. *J. Vac. Sci. Technol.* **13**, 188–194 (1995).
26. Hein, J. *et al.* Diode-pumped chirped pulse amplification to the joule level. *Appl. Phys. B* **79**, 419–422 (2004).
27. Mourou, G. A. & Umstadter, D. Extreme light. *Sci. Am.* **286**, 80–86 (2002).
28. Thomson, J. J. Rays of positive electricity. *Phil. Mag.* **21**, 225–249 (1911).
29. Rusch, G., Winkel, E., Noll, A. & Heinrich, W. The Siegen automatic measuring system for track detectors. *New developments. Nucl. Tracks Radiat. Meas.* **19**, 261–265 (1991).
30. Augst, S., Meyerhofer, D. D., Strickland, D. & Chint, S. L. Laser ionization of noble gases by Coulomb-barrier suppression. *J. Opt. Soc. Am. B* **8**, 858–867 (1991).

Supplementary Information is linked to the online version of the paper at www.nature.com/nature.

Acknowledgements We acknowledge the expert support of the Trident laser team, especially R. Johnson, T. Ortiz and R. Gonzales, and the target fabrication support from LANL group MST-7, particularly R. Perea. This work was supported by the LANL Laboratory Directed Research & Development (LDRD) programme. One of the authors (H.R.) was supported by DOE/NNSA-UNR and another (J.S.) by DFG and BMBF.

Author Contributions B.M.H. conceived the experiment. B.M.H., J.C., S.L. and J.C.F. executed the experiment. B.M.H., J.S., K.F. and J.C.F. analysed the data. H.R., B.J.A. and B.M.H. did the theory. M.P. and R.K.S. helped with the material science part and palladium surface chemistry, and B.M.H., B.J.A. and J.C.F. wrote the paper.

Author Information Reprints and permissions information is available at npg.nature.com/reprintsandpermissions. The authors declare no competing financial interests. Correspondence and requests for materials should be addressed to B.M.H. (hegelich@lanl.gov).

LETTERS

Laser-plasma acceleration of quasi-monoenergetic protons from microstructured targets

H. Schwoerer[1], S. Pfotenhauer[1], O. Jäckel[1], K.-U. Amthor[1], B. Liesfeld[1], W. Ziegler[1], R. Sauerbrey[1], K. W. D. Ledingham[1,2,3] & T. Esirkepov[4,5]

Particle acceleration based on high intensity laser systems (a process known as laser–plasma acceleration) has achieved high quality particle beams that compare favourably with conventional acceleration techniques in terms of emittance, brightness and pulse duration[1–4]. A long-term difficulty associated with laser–plasma acceleration—the very broad, exponential energy spectrum of the emitted particles—has been overcome recently for electron beams[5–7]. Here we report analogous results for ions, specifically the production of quasi-monoenergetic proton beams using laser–plasma accelerators. Reliable and reproducible laser-accelerated ion beams were achieved by intense laser irradiation of solid microstructured targets. This proof-of-principle experiment serves to illuminate the role of laser-generated plasmas as feasible particle sources. Scalability studies show that, owing to their compact size and reasonable cost, such table-top laser systems with high repetition rates could contribute to the development of new generations of particle injectors that may be suitable for medical proton therapy[8–10].

Beams of electrons, protons, ions and high energy photons produced by the interaction of ultraintense, ultrashort laser pulses with matter have received considerable attention throughout the last few years because of their high beam quality and their extensive potential for applications in science and technology[8–10].

The interaction of an intense light field with matter yields the generation of a hot plasma and the subsequent acceleration of electrons up to relativistic energies[11,12]. Protons and ions are accelerated by a well controlled mechanism known as 'target normal sheath acceleration' (TNSA)[13] following the initial electron acceleration (Fig. 1). Fast electrons are accelerated by an intense laser pulse (intensity $I \geq 10^{19}$ W cm^{-2}) from the surface of a thin metal foil in the forward direction. They penetrate the foil and ionize atoms along their paths. Within about a picosecond, those electrons leaving the target at the rear surface (that is, the back surface with respect to laser irradiation) build up a quasi-static electric field. The field acts normally to the target surface, has cylindrical symmetry and decreases in the transverse direction. Owing to the ultrashort duration of the electron bunch and its high charge, this field may reach values of several TV (10^{12} V) m^{-1} close to the axis and thus the potential can attain several tens of MeV (ref. 3). Protons and positively charged ions present on the back surface of the foil may be accelerated by this field until they compensate the electron charge. In most cases, the origin of these parasitic protons has been identified to be a hydrocarbon contamination layer on the target surface[14,15].

As the duration of the acceleration is ultrashort and the protons (as well as the ions) are at rest before acceleration, comprising a very small phase space volume, the transverse emittance of the proton beam reaches values as low as a few 10^{-3} mm mrad for 10 MeV protons[4]. However to date, laser accelerated ion beams still show a large longitudinal emittance, with their energy spectrum exhibiting a quasi-exponential shape with a distinct cut-off energy[1–3]. This can be explained by the inhomogeneous distribution of electrons in the sheath causing an accelerating field that is inhomogeneous in the transverse direction. For a plane and unstructured target, the transverse dimension of the electric field and hence the source size of accelerated protons are much larger than the laser's focal spot[16] (Fig. 1). Therefore, different parasitic protons experience a range of potentials, resulting in a broad distribution of energies.

Following this understanding of the mechanism of laser acceleration of protons, Bulanov *et al.*[10,17] pointed out that the resulting proton energy spectrum has a strong correlation to the spatial distribution of the protons on the target surface. In order to generate high quality proton beams with monoenergetic features, they proposed a bilayered, microstructured target, consisting of a thin high Z

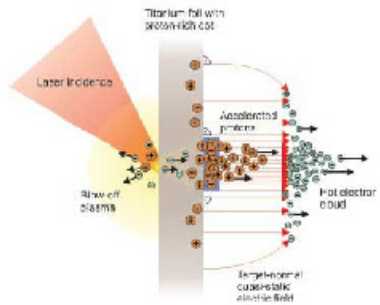

Figure 1 | Laser acceleration of protons from the back side of a microstructured target. A terawatt (TW)-laser pulse is focused onto the front side of the target foil, where it generates a blow-off plasma and subsequently accelerates electrons. The electrons penetrate the foil, ionize hydrogen and other atoms at the back surface and set up a Debye sheath. The inhomogeneous distribution of the hot electron cloud causes a transversely inhomogeneous accelerating field (target normal sheath acceleration—TNSA). Applying a small hydrogen-rich dot on the back surface enhances the proton yield in the central part of the accelerating field, where it is nearly homogenous. These protons constitute the quasi-monoenergetic bunch.

[1]Institut für Optik und Quantenelektronik, Friedrich-Schiller-Universität, 07743 Jena, Germany. [2]Department of Physics, University of Strathclyde, Glasgow G4 0NG, UK. [3]AWE plc, Aldermaston, Reading RG7 4PR, UK. [4]Kansai Research Establishment, JAERI, Kizu, Kyoto, 619-0215, Japan. [5]Moscow Institute of Physics and Technology, Dolgoprudny, 141700, Russia.

metal foil and a small proton-rich dot on the back surface. The transverse dimension of such dots is smaller than that of the acceleration sheath, and hence the protons will only be subject to the central—that is, homogeneous—part of the acceleration field. In this configuration, the protons all experience the same electric field and are accelerated in the same potential (Fig. 1). The resulting proton beam has a spectrum with a strong monoenergetic peak.

Here we present experimental results of a laser accelerated proton beam with a peaked energy distribution. The experimental arrangement follows the proposal in ref. 17 to use microstructured targets (Fig. 2). The results are well reproduced by two-dimensional particle-in-cell (PIC) simulations. The simulations also show the scalability of the technique.

The high intensity laser pulses (intensity $I = 3 \times 10^{19}\,\mathrm{W\,cm^{-2}}$) are generated by the JETI 10 TW Ti:sapphire laser at the University of Jena. It delivers pulses of 80 fs duration, a pulse energy of 600 mJ on target and a maximum repetition rate of 10 Hz. The target is a 5 μm thin titanium foil, coated with a 0.5 μm layer of polymethyl methacrylate (PMMA) on the back surface. In some regions of the sample the PMMA layer was microstructured, leaving PMMA dots of $(20 \times 20)\,\mu\mathrm{m}^2$ on the surface with PMMA-free space around (Fig. 2b). The laser pulse hits the foil on the front surface exactly opposite to one of the dots. Protons and ions, accelerated from the back surface in the normal direction, were analysed by a Thomson spectrometer and detected either by an online system based on microchannel plates (MCP) or by nuclear track detectors (CR39).

Figure 3 presents the result of irradiating the microstructured target foil at the position of a dot in contrast to unstructured material. The data are given as number of protons per energy interval of 0.05 MeV, which corresponds to our MCP resolution, and per 24 msr, which is the solid angle of emission, that results from the simulations described below. The curve indicated by the blue triangles shows the proton spectrum after irradiating a dot. It exhibits a distinct narrow band feature, peaked around $E_{max} = 1.2$ MeV on top of a broad, exponential shaped background. The displayed feature contains about 10^6 protons per 24 msr, and has a full-width at half-maximum of about $\Delta E_{FWHM} = 300$ keV or 25% of its absolute value. For comparison, the black data represent an average over six proton spectra recorded if the laser hits a blank position on the same target, where protons can only originate from an unstructured hydrogen contamination layer (parasitic protons). No narrow band feature appears, and the exponential shape of the spectrum can be approximated by a temperature of about 0.5 MeV. The occurrence of the peaked spectrum after irradiating a dot was also observed using CR39 detection. In the inset in Fig. 3, spectra obtained with the two detection methods are compared under the same conditions. Red circles and black squares represent spectra using MCP and CR39 detection, respectively. The two curves exhibit the same shape with a peak at 1.2 MeV, which accounts both for the reproducibility of generating peaked spectra as well as the reliability of the MCP detection. The proton yield at spectrum maximum is determined not only by the number of abundant protons in the dot but also by the laser characteristics, which affect the transverse scale of the electrostatic potential, the acceleration time and the spatial distribution of protons.

Owing to the limited size of the multichannel plate, the spectral range of the MCP data is smaller than that of the CR39 data sets. However, following direct successful comparison of these measurements, the electronic system provides a reliable online observation which allows for systematic investigation of the reproducibility with respect to proton yield, peak position and spectral width as well as for fast and controlled changes of experimental conditions. This experimental accuracy can only be accomplished with table-top lasers with high repetition rate. A maximum in the proton spectrum is reproduced consistently if a microstructure on the rear of the target is irradiated. The position of the peak E_{max} as well as its width ΔE_{FWHM} vary from shot to shot by ±20%.

From systematic experiments performed earlier on non-microstructured targets, it is known that an optimum target thickness with respect to maximum proton energy and yield follows from a given temporal structure of the laser pulse[18]. Considering our laser and target conditions, the exponential contribution to the proton distribution from the non-microstructured targets is in agreement with previously published results from similar targets[18–20].

The narrow band spectra of the laser accelerated protons observed in our experiments are due to the small proton-rich area within the centre of the larger quasi-static electric field, set up by the laser accelerated electrons beyond the thin target (Fig. 1). If the scale of the inhomogeneity of the electric field is larger than the proton-rich spot, these protons all experience the same potential. The maximum proton energy is determined by the total charge of electrons constituting the acceleration sheath and occurs on the axis, which in turn depends on the laser intensity and the target thickness[1]. This analysis is supported by two-dimensional PIC multi-parametric simulations based on the code REMP and the model of ref. 20: Fig. 4 plots the resulting proton spectrum (solid line) under the conditions laser intensity $I = 3 \times 10^{19}\,\mathrm{W\,cm^{-2}}$ and a 5 μm thin titanium target with 20 μm PMMA structure on the back side, which match the experimental parameters. The numerically achieved proton spectrum is dominated by a narrow band structure around 1.2 MeV with a full-width at half-maximum FWHM = 0.3 MeV or 25%. Simulation and experiment are in good agreement with respect to both the existence of the narrow structure as well as its position and width.

It was estimated[10,17] that in the case of a 10 μm focal spot and 0.1 μm thick proton layer, a proton energy spread of 1% can be expected. Furthermore, for microstructured targets the maximum proton energy (E_{max} in MeV) scales as the square root of the laser power (P, in PW) with $E_{max} = 230 \times P^{1/2}$ (refs 21, 22). The parameters for the simulation have been changed to smaller dot sizes and higher energies in order to extrapolate the technique to future experiments and investigate the scalability of our results (see Fig. 4 inset). A high repetition rate table-top laser system with petawatt power (POLARIS) will be available within a few years[23]. This laser will deliver pulses of 150 J within 150 fs, which leads to an intensity of about $10^{21}\,\mathrm{W\,cm^{-2}}$ in focus. Simulations performed with these parameters result in a peak proton energy at 173 MeV and relative width $\Delta E/E \approx 1\%$ for a dot diameter of 2.5 μm and a reduced layer thickness of 0.1 μm. Under these conditions, the proton yield is not longer limited by laser energy, but all protons contained in the dot (8×10^8) are quickly accelerated to an energy of 173 ± 1 MeV.

Proton beams with such a characteristic might be suitable for treatment of deep sited tumours[10]. More realistic within a few years is the potential for laser induced proton therapy for eye tumours, which only requires 60–70 MeV protons[24].

We have indicated that this experiment was carried out as 'proof of principle'. An extensive programme is now underway to reduce the width and increase the energy of our proton peaks by improving the target fabrication procedure. We intend to reduce the dimensions of the dots and change the target material. Our initial targets were dots on titanium, which was chosen on the basis of our preliminary experiments. Gold is expected to be a much better substrate[17], as it can deliver more electrons. In the Methods section, we describe how a Nd:YAG laser was used to reduce the thickness of the parasitic (contamination) layers by laser ablation[25]. Also, the same laser illuminated the dots to align their position with respect to the focal region. This straightforward optical positioning will allow future operation of the set-up at high repetition rate.

We have demonstrated the feasibility of laser–plasma accelerators for producing proton spectra with a reproducible monoenergetic peak using microstructured targets. Because of the high spectral density, all accelerated protons can be allocated to the respective application with high conversion efficiency. Our first steps towards monoenergetic protons show a distinct improvement over the exponential energy spectra published to date, heralding new possibilities for ion injectors and compact accelerators. In the longer term, future laser accelerators may be in reach of medical proton and heavy ion therapy.

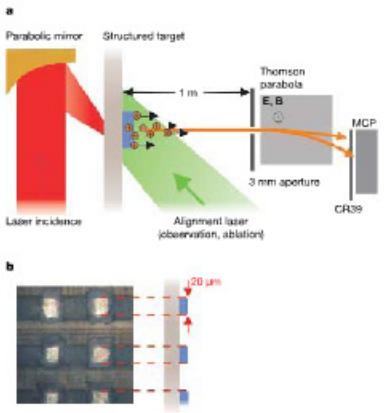

Figure 2 | Experimental and target arrangement for laser proton acceleration from microstructured targets. a, Experimental set-up: a TW-laser pulse is focused by a 45° off-axis parabolic mirror (f/2.5) to an intensity of $3 \times 10^{19}\,\mathrm{W\,cm^{-2}}$. A dot on the back surface of the target foil is positioned opposite to the focus using an alignment laser. A titanium foil of 5 μm thickness carries dots of PMMA with a thickness of 0.5 μm and a transverse size of 20 μm × 20 μm. The photograph of the microstructured back surface in **b** shows the dots as light squares. The protons and ions accelerated from the target are dispersed with respect to energy and charge-to-mass ratio in a Thomson parabola, and then detected by either a microchannel plate (MCP) with phosphor screen and CCD camera or on nuclear track detector plastics (CR39). A 3 mm lead aperture in front of the Thomson parabola serves as a pinhole for the Thomson spectrometer and additionally shields the MCP from bremsstrahlung.

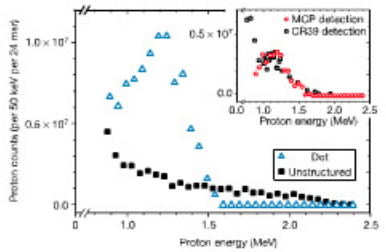

Figure 3 | Proton spectra from the Thomson spectrometer. The proton number reaching the detector is given per energy interval of 0.05 MeV and per solid angle of 24 msr versus proton energy. The main graph shows a spectrum obtained from irradiating the foil at the position of a dot using the MCP detection. It is represented by blue triangles. The spectrum from a dot exhibits a peak at an energy of 1.2 MeV as opposed to exponential spectra (black squares, average from six shots) in the case of using an unstructured part of the target foil. The peaked structure contains about 10^6 protons per 24 msr. The inset shows the comparison of the two detection systems: both spectra show the energy distribution of the protons from irradiating a dot under the same conditions. Red circles represent MCP detection, while black squares originate from CR39 detection.

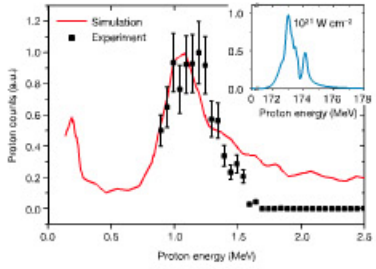

Figure 4 | Results from simulations and scalability of the technique. Comparison of experimental data (black squares) to the proton spectrum obtained from two-dimensional-PIC simulation (red line) for following conditions: laser intensity $I_L = 3 \times 10^{19}\,\mathrm{W\,cm^{-2}}$, and target dimensions 5 μm Ti foil + 0.5 μm PMMA dot (20×20) μm^2. Experimental data points comprise the observable energy range on the MCP detector. The statistical uncertainty for the measured data has a value of 20% s.d. as shown by the error bars. In the inset a simulation for a petawatt-laser system demonstrating the scalability of proton acceleration from microstructured targets is shown. The parameters for the simulation are $I_L = 1.2 \times 10^{21}\,\mathrm{W\,cm^{-2}}$, 5 μm Ti foil + 0.1 μm PMMA dot (2.5 μm diameter). The proton spectrum exhibits a narrow peak with relative energy width of $\Delta E/E = 1\%$ at a peak energy of 173 MeV.

METHODS

Laser. The experiments were performed using the JETI laser, a multi-TW Ti:sapphire laser system based on chirped pulse amplification. It delivered laser pulses containing 600 ± 25 mJ on target within a pulse duration of 80 ± 5 fs (1 fs = 10^{-15} s). The pulse duration was determined using a background-free THG autocorrelator and a Mach–Zehnder pulse front interferometer. Additionally, the amplified spontaneous emission was suppressed to a contrast of 10^9:1 at a time of 0.5 ps before the arrival of the main laser pulse using a fast Pockels cell. JETI operates at a centre wavelength of 795 nm and delivers a maximum of 10 shots per second. The laser parameters were fully characterized and monitored during the experiment. The laser pulses were focused by a 45° off-axis parabolic mirror (f/2.5) to a focal spot size of 7 μm^2 (radius $r = 1.5$ μm), yielding an intensity of $3 \times 10^{19}\,\mathrm{W\,cm^{-2}}$.

Target. In the experiments presented here, the solid state target was a 5 μm thin titanium foil, which was coated on one side (the back side with respect to laser irradiation) with a 0.5 μm thin layer of PMMA doped with Rhodamine 6G. The suitable thicknesses of the metal foil (5 μm) as well as the PMMA layer (0.5 μm) with respect to proton energy and proton number was determined in preliminary experiments. The 5 μm titanium foil was chosen for reasons of stability and reproducibility, even though thinner metal foils (2 μm) resulted in higher proton energies. The hydrogen-rich PMMA layer was microstructured by means of femtosecond laser ablation, yielding dots with a size of $(20 \times 20)\,\mu\mathrm{m}^2$ with a 'PMMA-free' space of 30 μm in between, see Fig. 2b. The target was stretched in a rigid frame to ensure optimal flatness and moved before each shot to an unirradiated, that is, intact, area. In the key part of the experiments each laser pulse was launched on the front side of the target exactly opposite to one of the dots. This was accomplished by localizing the dots with help of a frequency doubled Nd:YAG laser (532 nm) and observing the yellow fluorescence light (around 600 nm) of the dot. The foci of the TW pulse and the Nd:YAG laser were aligned to overlap in space. The dot's position, determined from the back side,

was brought into spatial coincidence with the position of the focal spot on the front side. An additional effect of the irradiation of the target's back surface with the Nd:YAG laser was a reduction of the parasitic proton layer by laser ablation before the high intensity laser struck the target.

Proton detection. Protons and ions accelerated from the foil were detected either by a chevron microchannel plate (MCP) with phosphor screen and CCD camera or on nuclear track detector CR39. Before hitting the detector, the proton/ion beam traversed a Thomson parabola type spectrometer comprising a magnetic field ($B = 535$ mT) parallel to an electric field ($E_{max} = 2{,}500$ V cm^{-1}). Thus, the proton/ion beam was dispersed with respect to energy and charge-to-mass ratio. The energy distribution was then determined from the spatial distribution of the protons on the detector. The MCP system has the major advantage of providing real time detection. It was carefully calibrated by a comparison of pixel counts to proton pits on a piece of CR39. The energy spectra from MCP and CR39 are measured with an energy resolution of 50 keV, which corresponds to the resolution of the MCP, and per solid angle of 10 μsr defined by the 3 mm aperture in front of the Thomson parabola. The spectra are scaled to 24 msr, which is the full angle of emission as obtained from the simulation.

Received 14 September; accepted 1 December 2005.

1. Maksimchuk, A., Gu, S., Flippo, K., Umstadter, D. & Bychenkov, V. Forward ion acceleration in thin films driven by a high-intensity laser. *Phys. Rev. Lett.* **84**, 4108–4111 (2000).
2. Clark, E. *et al.* Measurement of energetic proton transport through magnetized plasma from intense laser interactions with solids. *Phys. Rev. Lett.* **85**, 1654–1657 (2000).
3. Snavely, R. A. *et al.* Intense high-energy proton beams from petawatt-laser irradiation of solids. *Phys. Rev. Lett.* **85**, 2945–2948 (2000).
4. Cowan, T. E. *et al.* Ultralow emittance, multi-MeV proton beams from a laser virtual-cathode plasma accelerator. *Phys. Rev. Lett.* **92**, 204801 (2004).
5. Mangles, S. *et al.* Monoenergetic beams of relativistic electrons from intense laser-plasma interactions. *Nature* **431**, 535–538 (2004).
6. Geddes, C. *et al.* High-quality electron beams from a laser wakefield accelerator using plasma-channel guiding. *Nature* **431**, 538–541 (2004).
7. Faure, J. *et al.* A laser-plasma accelerator producing monoenergetic electron beams. *Nature* **431**, 541–544 (2004).
8. Tajima, T. & Mourou, G. Zetawatt-exawatt lasers and their applications in ultrastrong-field physics. *Phys. Rev. Spec. Topics Accelerators Beams* **5**, 031301 (2002).
9. Ledingham, K. W. D., McKenna, P. & Singhal, R. P. Applications for nuclear phenomena generated by ultra-intense lasers. *Science* **300**, 1107–1111 (2003).
10. Bulanov, S. & Khoroshkov, V. Feasibility of using laser ion accelerators in proton therapy. *Plasma Phys. Rep.* **28**, 453–456 (2002).
11. Modena, A. *et al.* Electron acceleration from the breaking of relativistic plasma waves. *Nature* **377**, 606–608 (1995).
12. Malka, V. *et al.* Electron acceleration by a wake field forced by an intense ultrashort laser pulse. *Science* **298**, 1596–1600 (2002).
13. Wilks, S. *et al.* Energetic proton generation in ultra-intense laser-solid interactions. *Phys. Plasmas* **8**, 542–549 (2001).
14. Gitomer, S. J. *et al.* Fast ions and hot-electrons in the laser-plasma interaction. *Phys. Fluids* **29**, 2679–2688 (1986).
15. Hegelich, M. *et al.* MeV ion jets from short-pulse-laser interaction with thin foils. *Phys. Rev. Lett.* **89**, 085002 (2002).
16. Schreiber, J. *et al.* Source-size measurements and charge distributions of ions accelerated from thin foils irradiated by high-intensity laser pulses. *Appl. Phys. B* **79**, 1041–1045 (2004).
17. Esirkepov, T. *et al.* Proposed double-layer target for the generation of high quality laser accelerated ion beams. *Phys. Rev. Lett.* **89**, 175003 (2002).
18. Kaluza, M. *et al.* Influence of the laser prepulse on proton acceleration in thin-foil experiments. *Phys. Rev. Lett.* **93**, 045003 (2004).
19. Spencer, I. *et al.* Experimental study of proton emission from 60-fs, 200-mJ high-repetition-rate tabletop-laser pulses interacting with solid targets. *Phys. Rev. E* **67**, 046402 (2003).
20. Matsukado, K. *et al.* Energetic protons from a few-micron metallic foil evaporated by an intense laser pulse. *Phys. Rev. Lett.* **91**, 215001 (2003).
21. Bulanov, S. V. *et al.* Feasibility of using laser acceleration in proton therapy. *AIP Conf. Proc.* **740**, 414–429 (2004).
22. Esirkepov, T. *et al.* Laser ion acceleration scaling laws seen in multi-parametric PIC simulations. *Phys. Rev. Lett.* (submitted); preprint at (http://arxiv.org/abs/physics/0510189) (2005).
23. Hein, J. *et al.* Diode-pumped chirped pulse amplification to the joule level. *Appl. Phys. B* **79**, 419–422 (2004).
24. Damato, B., Kacperek, A., Chopra, M., Campbell, I. R. & Errington, R. D. Proton beam radiotherapy of choroidal melanoma: The Liverpool-Clatterbridge experience. *Int. J. Radiat. Oncol. Biol. Phys.* **62**, 1405–1411 (2005).
25. Allen, M. *et al.* Direct experimental evidence of back-surface ion acceleration from laser-irradiated gold foils. *Phys. Rev. Lett.* **93**, 265004 (2004).

Acknowledgements This work was supported by the Deutsche Forschungsgemeinschaft. T.E. thanks S. V. Bulanov for discussions. K.W.D.L. takes pleasure in the receipt of a Carl-Zeiss visiting professorship. We thank F. Ronneberger and B. Beleites for their technical support. We thank H.-J. Fuchs and W. Grätf for their help in producing the targets.

Author Information Reprints and permissions information is available at npg.nature.com/reprintsandpermissions. The authors declare no competing financial interests. Correspondence and requests for materials should be addressed to H.S. (schwoerer@ioq.uni-jena.de).

LETTERS

Amplification of chirality in two-dimensional enantiomorphous lattices

Roman Fasel[1], Manfred Parschau[1] & Karl-Heinz Ernst[1]

The concept of chirality dates back to 1848, when Pasteur manually separated left-handed from right-handed sodium ammonium tartrate crystals[1]. Crystallization is still an important means for separating chiral molecules into their two different mirror-image isomers (enantiomers)[2], yet remains poorly understood[3]. For example, there are no firm rules to predict whether a particular pair of chiral partners will follow the behaviour of the vast majority of chiral molecules and crystallize together as racemic crystals[4], or as separate enantiomers. A somewhat simpler and more tractable version of this phenomenon is crystallization in two dimensions, such as the formation of surface structures by adsorbed molecules. The relatively simple spatial molecular arrangement of these systems makes it easier to study the effects of specific chiral interactions[5]; moreover, chiral assembly and recognition processes can be observed directly and with molecular resolution using scanning tunnelling microscopy[6–9]. The enantioseparation of chiral molecules in two dimensions is expected to occur more readily because planar confinement excludes some bulk crystal symmetry elements and enhances chiral interactions[10,11]; however, many surface structures have been found to be racemic[12–18]. Here we show that the chiral hydrocarbon heptahelicene on a Cu(111) surface does not undergo two-dimensional spontaneous resolution into enantiomers[19], but still shows enantiomorphism on a mesoscopic length scale that is readily amplified. That is, we observe formation of racemic heptahelicene domains with non-superimposable mirror-like lattice structures, with a small excess of one of the heptahelicene enantiomers suppressing the formation of one domain type. Similar to the induction of homochirality in achiral enantiomorphous monolayers[20] by a chiral modifier, a small enantiomeric excess suffices to ensure that the entire molecular monolayer consists of domains having only one of two possible, non-superimposable, mirror-like lattice structures.

Mixtures of M- and P-enantiomers of the helically shaped heptahelicene ($C_{30}H_{18}$, [7]H, Fig. 1a) have been deposited onto the (111)-surface of a copper single crystal (Supplementary Methods). The scanning tunnelling microscope (STM) image for a closed-packed molecular layer of racemic [7]H on Cu(111) in Fig. 1b shows extended two-dimensional (2D) domains with a diameter limited mainly by the terrace width of the underlying substrate surface (~50 nm). Enantiomorphism is manifested by the oblique alignment of the adsorbate lattice, which destroys the reflection symmetry of the underlying substrate. The lattice vectors of the two mirror-domains λ and ρ are tilted by opposite angles of $\pm 10.9°$ with respect to the $[1\bar{1}0]$ substrate surface direction. This 2D enantiomorphism has previously been observed by means of low energy electron diffraction (LEED)[19] and attributed to spontaneous resolution of the mixture into homochiral domains. However, the present STM observations reveal that the local molecular arrangement within the two domains

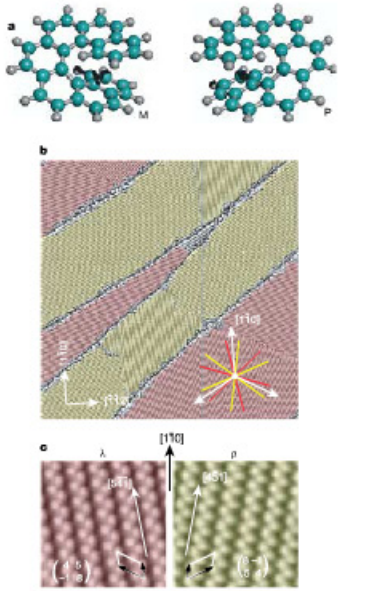

Figure 1 | Enantiomorphous domains of racemic heptahelicene on Cu(111). a, Ball and stick model of the two enantiomers of heptahelicene (green, carbon; grey, hydrogen). **b**, STM image (200×200 nm^2) showing the formation of extended close-packed domains. Left- (λ) and right-handed (ρ) domains are coloured red and yellow, respectively. **c**, Close-up images (10×10 nm^2) of the two mirror domains reveal zigzag rows running along the [54$\bar{1}$] (λ) and [45$\bar{1}$] directions (ρ), forming angles of $\mp 10.9°$ with respect to the close-packed $[1\bar{1}0]$ surface directions. The $\begin{pmatrix} 4 & 5 \\ -1 & 8 \end{pmatrix}$ (λ domain) and $\begin{pmatrix} 8 & -1 \\ 5 & 4 \end{pmatrix}$ (ρ domain) unit cells are indicated.

[1]Empa, Swiss Federal Laboratories for Materials Testing and Research, Überlandstrasse 129, CH-8600 Dübendorf, Switzerland.